28th Symposium on Naval Hydrodynamics
Pasadena, California, 12-17 September 2010

Large Eddy Simulation of Marine Propulsors in Crashback

Hyunchul Jang, Krishnan Mahesh
(Aerospace Engineering and Mechanics, University of Minnesota)

ABSTRACT

Flow around a marine propulsor under crashback operating condition is computed using the large eddy simulation methodology. The incompressible Navier-Stokes equations are simulated in a rotating frame of reference that rotates with the propulsor. A non-dissipative and robust finite volume method developed by Mahesh et al. (2004) is used on unstructured grids. The simulation yields good mean values of unsteady loads as compared to experiments. Also, good agreement with experimental results is observed in circumferentially averaged flow fields. Time averaged flow fields are further investigated. Two quantities for pressure contributions to thrust and side-force are introduced to more clearly understand where thrust and side-force originate. Thrust and side-force are seen to be mainly generated from the suction side of the leading edge of propulsor blades. Conditional averages are performed to obtain quantitative information about the complex flow physics of high or low thrust and high or low side-force.

INTRODUCTION

Crashback is an operating condition where the propulsor rotates in the reverse direction while the vessel moves in the forward direction. Since the crashback condition is dominated by large scale unsteadiness, it is well known as one of the most challenging to analyze. Low frequency components of the unsteadiness can affect propulsor thrust, torque, and side-force, which affect maneuverability of the vessel during crashback condition.

The crashback condition is dominated by the interaction of the free stream flow with the strong reversed flow from propulsor rotation as shown in figure 1. This interaction forms the unsteady ring vortex that is the most remarkable aspect of the flow during crashback operation.

Jiang et al. (1996) studied the structure of the unsteady vortex ring using Particle Image Velocimetry (PIV) measurements. They noted that the unsteady vortex ring is related to unsteady shaft forces and the oscillation frequency of the ring vortex is much lower than the propulsor rotation rate. Jessup et al. (2004) presented more detailed measurements of flow velocity fields using PIV and Laser Doppler Velocimetry (LDV).

The computational prediction of the flow around marine propulsors has been performed using unsteady Reynolds-Averaged Navier-Stokes equations (RANS) (Chen & Stern, 1999; Davoudzadeh et al., 1997). They showed that RANS yielded good results for forward and backward modes, but produced significant discrepancies in crashback and crashahead modes.

The cross-section of a propulsor blade with the cylindrical surface resembles an airfoil. Under the crashback condition, the leading and trailing edges of propulsor blades exchange their roles. The sharp trailing edge of normal conditions becomes the leading edge so that large flow separations could occur at the sharp leading edge. The large flow separations may cause high amplitude fluctuation of unsteady loads. Large Eddy Simulation (LES) is therefore an attractive computational methodology for predicting the fluctuating forces. Since RANS is based on time average or ensemble average, it cannot accurately predict high fluctuation of unsteady loads.

Mahesh et al. (2004) developed a non-dissipative and robust finite volume method with LES on unstructured grids. Vyšohlíd & Mahesh (2006) performed numerical simulations of crachback condition with the code at the advance ratio J=-0.7. They showed that LES could yield good agreement for mean and RMS values of unsteady loads. Also, circumferentially average flow fields from the computation were compared to experiments, but predicted the center of the recirculation zone was closer to propulsor blades.

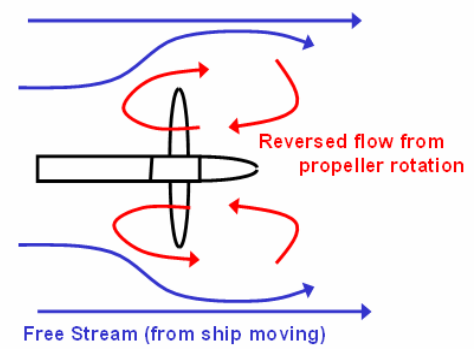

Figure 1. Schematic of crashback condition.

Chang et al. (2008) performed LES at other advance ratio, J=-0.5 and J=-1.0 with the same LES code and computational grid as Vyšohlíd & Mahesh (2006). They investigated instantaneous flow fields at a high thrust event and a low thrust event to understand the physics of crashback. They reported that a bi-modal behavior with vortex ring and axial jet modes occurred at low negative J. At high negative J, the flow only acted in ring vortex mode.

In this paper, we compute the flow at J=-0.7 with a new improved computational grid. The present simulation with the new grid shows good agreement with experimental data in circumferentially averaged flow fields. Two quantities for pressure contributions to thrust and side-force are introduced to more clearly understand where thrust and side-force originate. We also use conditional averaging to study the flow field.

SIMULATION DETAILS

Numerical Method

Simulations are performed in a frame of reference that rotates with the propulsor. The incompressible Navier-Stokes equations in the rotating frame of reference can be formulated in a strongly conservative form (Beddhu et. al., 1996) or in a form where system rotation produces a source term (Majety, 2003). Also, the governing equations can either be written for the absolute velocity vectors in the stationary frame or for the relative velocity vectors in rotating frame. Here, the rotational source term is chosen with the absolute velocity vectors for convenience to handle boundary conditions as follows.

$$\frac{\partial u_i}{\partial t}+\frac{\partial}{\partial x_j}(u_i u_j - u_i \varepsilon_{jkl}\omega_k x_l) = -\frac{\partial p}{\partial x_i}-\varepsilon_{ijk}\omega_j u_k + \nu\frac{\partial^2 u_i}{\partial x_j \partial x_j} \qquad (1)$$
$$\frac{\partial u_i}{\partial x_i}=0$$

where u_i are the inertial velocities in the stationary frame, p is the pressure, x_i are coordinates in the rotating non-inertial reference frame, ω_j is the angular velocity of the rotating frame of reference, ν is the kinematic viscosity, and ε_{ijk} denotes the permutation symbol for the tensor notation.

In LES, large unsteady motions are directly solved with spatially filtered equations, whereas effects of small scale motions are modeled. The spatially filtered momentum equation in the initial reference frame is

$$\frac{\partial \overline{u}_i}{\partial t}+\frac{\partial}{\partial x_j}(\overline{u}_i \overline{u}_j) = -\frac{\partial \overline{p}}{\partial x_i}+\nu\frac{\partial^2 \overline{u}_i}{\partial x_j \partial x_j}-\frac{\partial \tau_{ij}}{\partial x_j} \qquad (2)$$
$$\frac{\partial \overline{u}_i}{\partial x_i}=0$$

where $\bar{}$ denotes the spatial filter and $\tau_{ij}=\overline{u_i u_j}-\overline{u}_i\overline{u}_j$ is the sub-grid stress. The sub-grid stress is modeled by dynamic Smagorinski model (Germano et al., 1991; Lilly, 1992).

In the rotating frame of reference, the additional rotational term are introduced in the filtered equations as in Eq. (1).

$$\frac{\partial \overline{u}_i}{\partial t}+\frac{\partial}{\partial x_j}(\overline{u}_i \overline{u}_j - \overline{u}_i \varepsilon_{jkl}\omega_k x_l) = -\frac{\partial \overline{p}}{\partial x_i}-\varepsilon_{ijk}\omega_j \overline{u}_k + \nu\frac{\partial^2 \overline{u}_i}{\partial x_j \partial x_j}-\frac{\partial \tau_{ij}}{\partial x_j} \qquad (3)$$
$$\frac{\partial \tilde{u}_i}{\partial x_i}=0$$

with an approximation $\overline{u_i \varepsilon_{jkl}\omega_k x_l} \approx \overline{u}_i \varepsilon_{jkl}\omega_k x_l$.

Eq. (3) are solved by a numerical method developed by Mahesh et al. (2004) for incompressible flows on unstructured grids. The algorithm is derived to be robust without numerical dissipation. It is a finite volume approach which stores the Cartesian velocities and the pressure at the centroids of the cells and the face normal velocities are stored independently at the centroids of the faces. A predictor-corrector approach is used. The predicted velocities at the control volume centroids are first obtained and then interpolated to obtain the face normal velocities. The predicted face

normal velocity is projected so that continuity is discretely satisfied. This yields a Poisson equation for pressure which is solved iteratively using a multigrid approach. The pressure field is used to update the Cartesian control volume velocities using a least-squared formulation. Time advancement is performed using an implicit Crank-Nicholson scheme. The algorithm has been validated for a variety of problems (Mahesh et al., 2004) over a range of Reynolds numbers.

Propulsor Geometry, Computational Mesh and Boundary Conditions

Simulations are performed for a marine propulsor P4381, which is a five-bladed, right-handed with variable pitch, no skew and rake. The propulsor has been used in various experiments (Jessup et al., 2004; Jessup et al., 2006; Jiang et al., 1997) and computations (Chen & Stern, 1999; Davoudzadeh et al., 1997; Vyšohlíd & Mahesh, 2006; Chang et al., 2008). The detailed propulsor geometry and hub geometry are given in Jessup et al. (2006).

The computational domain is a cylinder with the diameter of 7.0D and the length of 14.0D where D is the diameter of the propulsor disk. Free-stream velocity boundary conditions are specified at the inlet and the lateral boundaries. Convective boundary conditions are prescribed at the exit. As mentioned, boundary

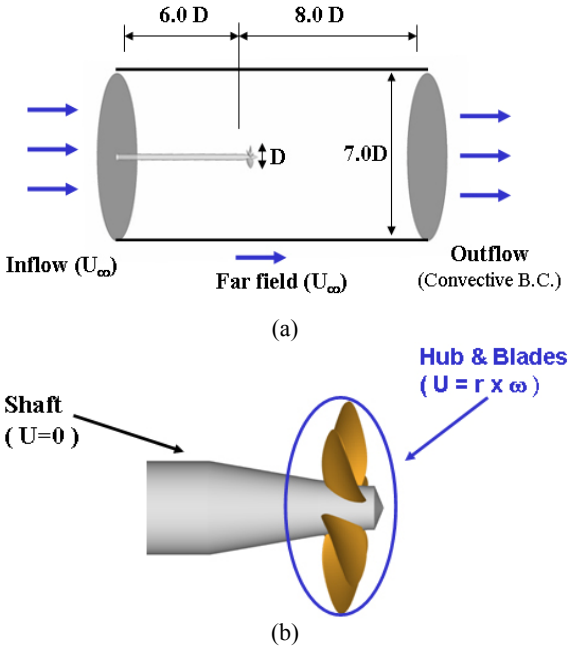

Figure 2. (a) Computational domain and boundary conditions on domain boundaries, (b) boundary conditions on solid walls.

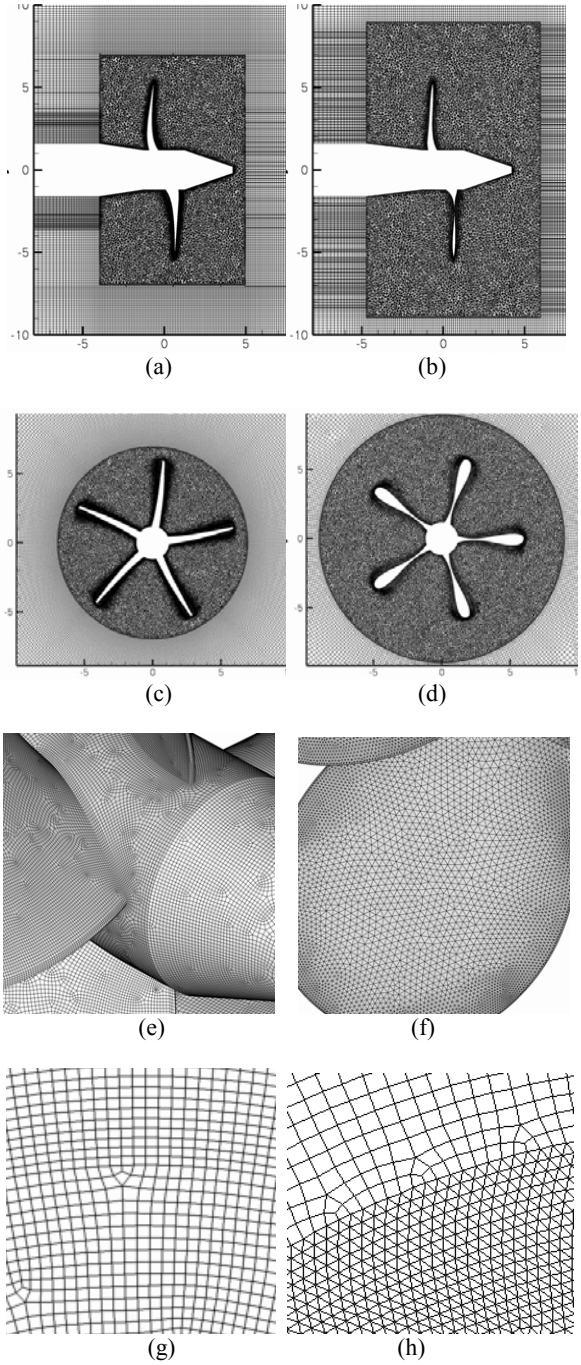

Figure 3. Comparisons of present and previous (Vyšohlíd & Mahesh, 2006) computational grids: (a) XY plane of new grid, (b) XY plane of previous grid, (c) x=0 plane of new grid, (d) x=0 plane of previous grid, (e) surface meshes of new grid, (f) surface meshes of previous grid, (g) surface meshes of the pillbox of new grid, (h) surface meshes of the pillbox of previous grid.

conditions on solid walls are forced as those are prescribed in the inertial reference frame. Thus, boundary conditions on rotor part, blades and hub, are specified as $u = \omega \times r$, while those on stator part are prescribed as no-slip boundary conditions. Schematics of the computational domain and boundary conditions are shown in figure 2(a) and 2(b).

Previous simulations with LES were performed by the same computational grid (Vyšohlíd & Mahesh, 2006; Chang et al., 2008). Even though the previous simulations have been performed with fairly good agreement in statistics of unsteady loads, they predicted that the center of recirculation zone is located quite closer to propulsor blades than Jessup et al. (2004)'s LDV data. So, the new computational grid is improved from three points of view.

First, the grid is created from the original CAD data of the propulsor P4381. Figure 3(a) and 3(c) show cross-sectional planes of the new grid. Figure 3(b) and 3(d) are cross-sections of the previous grid. The x=0 planes are obviously different from each other.

Second, all surfaces of the propulsor are meshed by quadrilateral elements instead of triangular elements. As shown in figure 3(e), surface meshes of the new grid are quadrilateral as compared to triangular elements in figure 3(f). Prism meshes extruded from those surfaces becomes hexahedral meshes so that more accurate solutions are expected. Also, surface meshes of the pillbox consist of quadrilateral elements. With this modification, hexahedral meshes are used for wake region instead of prism meshes. Figure 3(h) and 3(g) compare surface meshes of the pillbox in the new and old grids, respectively. Both triangular and quadrilateral meshes are used for the previous grid at boundaries of the pillbox in figure 3(h). But, only quadrilateral meshes are used for the present grid in figure 3(g).

Third, the size of the pillbox is made smaller. The pillbox is the cylindrical sub-domain where tetrahedral meshes are used to match complex geometries of blades. The size of the pillbox is shrunk as small as possible for the new computational grid. Figure 3(a) and 3(b) show comparison with pillbox sizes of present and previous grids.

The Table 1 lists information of present and previous (Vyšohlíd & Mahesh, 2006) computational grids. The number of elements is increased from 13.3 millions to 19.3 millions. However, the number of elements in the pillbox is not increased very much for the smaller sized pillbox. The minimum size of the grid spacing and the number of prism layers from blades do not change for the new grid.

	Present	Vyšohlíd & Mahesh (2006)
# of elements	19.3 mils	13.3 mils
# of meshes in pillbox (percentage)	6.1mils (31.8%)	5.4 mils (40.6%)
Min. grid spacing	0.0017D	0.0017D
Dimension of pillbox (diameter x height)	1.0D x 0.73D	1.5D x 0.92D

Table 1. Information of present and previous (Vyšohlíd & Mahesh, 2006) computational grids.

RESULTS

Simulations have been performed under the crashback condition at the advance ratio J = -0.7 and Reynolds number Re = 480,000. The advance ratio J and Reynolds number *Re* are defined as

$$J = \frac{U}{nD}, \quad \mathrm{Re} = \frac{DU}{\nu} \qquad (4)$$

where U is the free-stream velocity, n is the propulsor rotational speed, and D is the diameter of the propulsor disk. According to Jessup et al. (2004)'s experiments, thrust and torque do not depend on Reynolds number where $4\times10^5 < \mathrm{Re} < 9\times10^5$. The Reynolds number Re=480,000 is within this range.

For the present simulation, J = -0.7 is chosen because circumferentially averaged flow fields were measured with LDV by Jessup et al. (2004) and compared to LES results by Vyšohlíd & Mahesh (2006) at this advance ratio.

Time History of Unsteady Loads

The axial component of force is the thrust T and the axial component of moment of force is the torque Q. In addition, the projection of force onto the direction perpendicular to the propulsor axis is termed the side-force. Since computations are performed in the rotating frame of reference, the side-force is translated to the inertial reference frame. The horizontal and vertical components of the side-force, F_H and F_V, respectively, can be obtained from a rotational transformation using the angle between the rotating frame and the inertial frame.

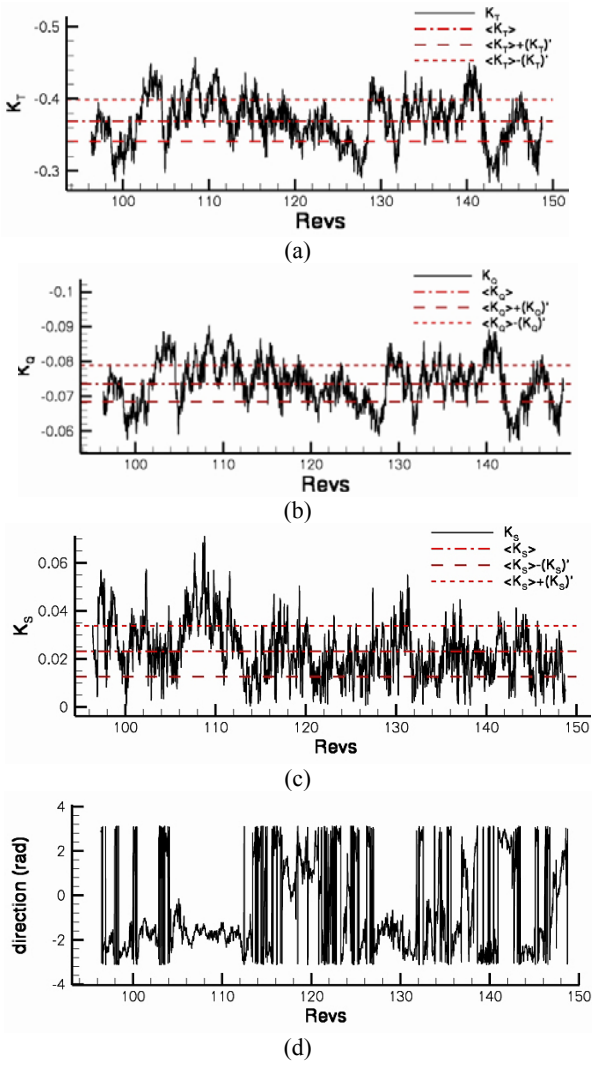

Figure 4. Time histories of unsteady loads: (a) thrust coefficient K_T, (b) torque coefficient K_Q, (c) side-force coefficient K_S, (d) side-force angle θ_S.

	$<K_T>$	$<K_Q>$	$<K_S>$
LES (present)	-0.37	-0.074	0.023
LES (2006)	-0.39	-0.073	0.025
WT (2004)	-0.33	-0.065	0.024
OW (2006)	-0.41	-0.078	-

Table 2. Mean values of K_T, K_Q, and K_S.

Non-dimensional thrust coefficient K_T, torque coefficient K_Q, side-force coefficient K_S, and side-force angle θ_S are given by

$$K_T = \frac{T}{\rho n^2 D^4}, \quad K_Q = \frac{Q}{\rho n^2 D^5}$$
$$K_S = \frac{\sqrt{F_H^2 + F_V^2}}{\rho n^2 D^4}, \quad \theta_S = \tan^{-1}\left(\frac{F_V}{F_H}\right) \tag{5}$$

where T is thrust, Q is torque, F_H is horizontal side-force, F_V is vertical side-force, and ρ is the density of the fluid.

The time histories of K_T, K_Q, K_S, and θ_S are shown in figure 3(a)-(d), respectively. $<\cdot>$ denotes the mean value and $(\cdot)'$ denotes standard deviation. The horizontal lines in figure 3 are the mean and the mean plus or minus standard deviation. Since K_T is negative, $<K_T>-(K_T)'$ represents the high thrust and $<K_T>+(K_T)'$ means the low thrust. This is similarly applied to K_Q, but $<K_S>-(K_S)'$ represents the low side-force and $<K_S>+(K_S)'$ means the high side-force.

Table 2 compares computed mean values to the previous experiments and computation. In the table, WT denotes 36″-water tunnel experiment and OW is towing-tank experiment, and LES (2006) denotes the computation by Vyšohlíd & Mahesh (2006). The present LES predicts very similar mean values of K_T, K_Q, and K_S, but standard deviations are almost half of the previous experiment and computation. It might be because the number of revolutions is smaller than the previous ones. The experiments were performed for 700 revolutions and even the previous computation was performed over 300 revolutions.

Mean values of K_T and K_Q are located between water tunnel and towing-tank results. Since the size of the water tunnel is, however, only three times of the propulsor diameter, it may suffer from tunnel effect. Particularly, the ring vortex structure caused by crashback could interact with the tunnel surface due to the insufficient size of the water tunnel. On the other hands, towing-tank experiment does not have any tunnel effect, but only unsteady loads in the axial direction are measured in the experiment. So, the fact that computed mean values are located between WT and OW results is reasonable.

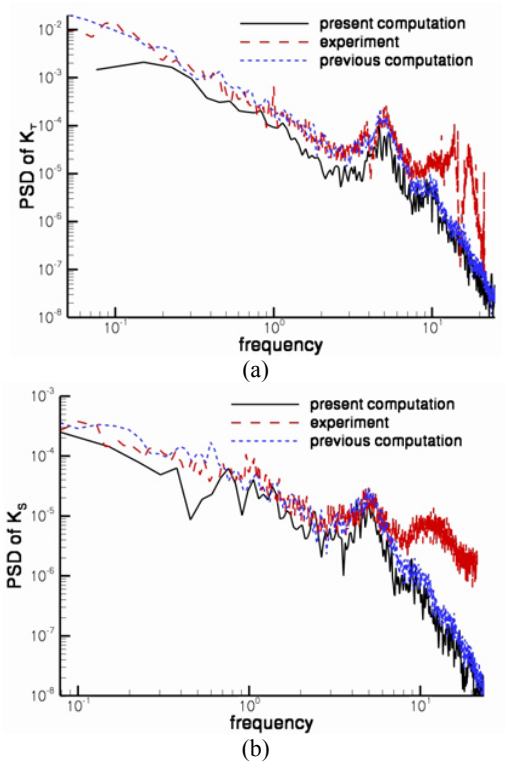

Figure 5. Power Spectral Density for unsteady loads: (a) K_T, (b) K_S.

.

Figure 5 shows the Power Spectral Density (PSD) of K_T and K_S for the water tunnel experiments, the present LES, and the previous LES. The PSD's are computed by dividing time histories of unsteady loads into N segments with 50% overlap. Each segment is filtered using the Hanning window to minimize end effects, rescaled to maintain the original energy, and transformed into spectral domain using the Fast Fourier Transform (FFT). The PSD computed for each segment are averaged over all segments. The PSD for the present computation is computed over 52.38 revolutions with 11,000 samples. The PSD for the experiment is given with around 700 revolutions and 30,000 samples. The PSD for the previous computation is obtained over about 300 revolutions with 50,500 samples.

All PSD's of two computations and experiment show the same peak at frequency 5 rev-1, which corresponds to the passage of blades of the five blades propulsor. Additional higher frequency peaks also exist only in the experimental PSD.

Time Averaged Flow Fields

The computed results are averaged in time over a period of 52.38 revolutions. The time-averaged flow fields measured with LDV by Jessup et al. (2004) are compared with the computational results. Since the LDV data were measured in X-R plane, the time-averaged fields are circumferentially averaged. The computational results are also compared with the previous LES results of Vyšohlíd & Mahesh (2006).

Figure 6 compares circumferentially averaged flow fields with experimental results and two computational results. Figure 6(a)-(b) are present LES results, figure 6(c)-(d) are Jessup et al.(2004)'s LDV results, and figure 6(e)-(f) are previous LES results of Vyšohlíd & Mahesh (2006). The center of the recirculation zone from the present computation is mostly coincident with that from the experimental data.

On the other hand, that from Vyšohlíd & Mahesh (2006)'s results is located in somewhat closer point to propulsor blades. Locations of centers of recirculation zones are listed in Table 3. As shown in figure 6, the center from the present computation is almost the same as that from experimental results. However, x_cen (x component of the center) from the previous computation is approximately half of x_cen from experimental results.

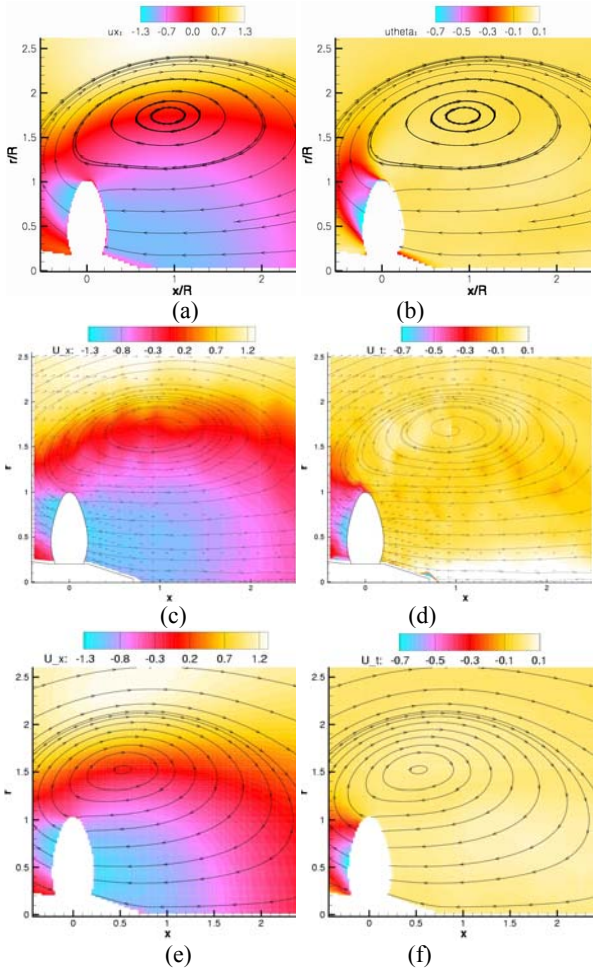

Figure 6. Circumferentially averaged flow fields: (a) axial velocity and (b) tangential velocity (LES; present), (c) axial velocity and (d) tangential velocity (experiment; Jessup et al., 2004), (e) axial velocity and (f) tangential velocity (LES; Vyšohlíd & Mahesh, 2006).

	x_cen / R	r_cen / R
LES (present)	0.93	1.75
LES (2006)	0.53	1.53
WT (2006)	0.96	1.71

Table 3. Locations of centers of recirculation zones of circumferentially averaged flow fields from computations and experiments

Axial velocities are plotted in figure 6(a), 6(c), and 6(e) (left). Blue colored zone in the neighborhood of blades means strongly reversed flow from propulsor rotation. This reversed flow interacts with surrounding free stream to create the vortex ring structure. The present computation and measured data show very good agreement. However, the previous computation predicts a smaller reversed flow region.

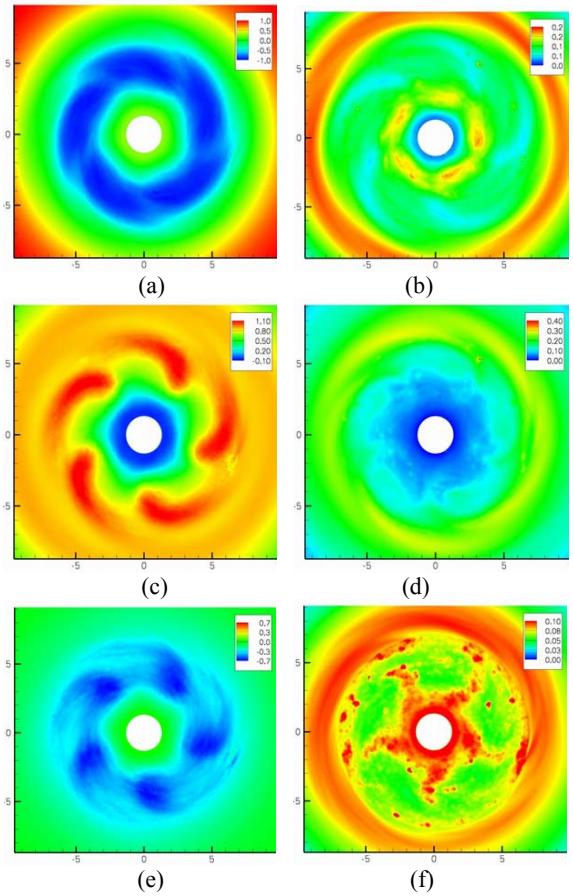

Figure 7. Time averaged flow fields at x/R = -0.33 (outflow of the propeller): (a) mean axial velocity, (b) RMS of axial velocity, (c) mean radial velocity, (d) RMS of radial velocity, (e) mean tangential velocity, (f) RMS of tangential velocity.

Figure 6(b), 6(d), and 6(f) (right) are tangential (circumferential) velocities. Since the propulsor rotates in negative circumferential direction, the tangential velocity is negative over almost entire field. Especially, downstream of the propulsor has strong negative tangential velocity. Both of the present computation and the experiment show larger strong negative region than the previous computation. Both results also show that the strong negative region is spread outside of the propulsor disk.

Overall, circumferentially average fields from the present computation show very good agreement with experimental results. Time-averaged flow fields from the present computation are used to understand the physics of crashback.

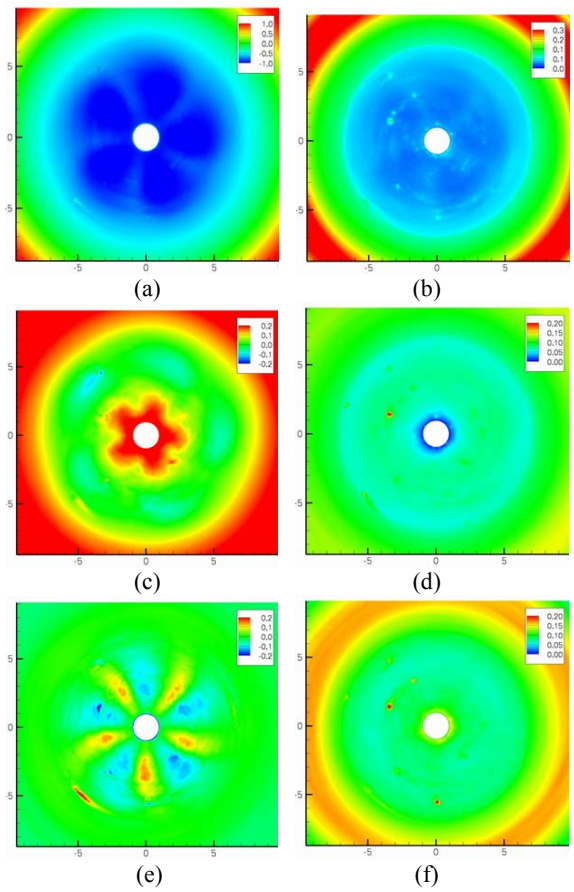

Figure 8. Time averaged flow fields at x/R = 0.33 (inflow of the propeller): (a) mean axial velocity, (b) RMS of axial velocity, (c) mean radial velocity, (d) RMS of radial velocity, (e) mean tangential velocity, (f) RMS of tangential velocity.

Time averaged flow fields at the outflow of the propulsor (x/R = -0.33) are plotted in figure 7. The axial velocity is strongly reversed in the range of 0.5 < r/R < 1.0 in figure 7(a). The RMS of the axial velocity is higher at the outside of the recirculation zone where the strong shear layer exists. The radial velocity to the outward direction is higher at the same radius range. The negative tangential velocity is found at the same location. In sum, strong reversed flow with negative swirling and outward motions exists in this radius range at the outflow.

Time averaged flow fields at the inflow of the propulsor (x/R = 0.33) are shown in figure 8. The axial velocity is strongly and uniformly reversed for entire radius range of the propulsor. The inward radial velocity is quite small. Positive and negative tangential velocities occur at neighborhoods of leading edges of blades. The uniform reversed flow with small radial and tangential velocities is the incoming flow of the

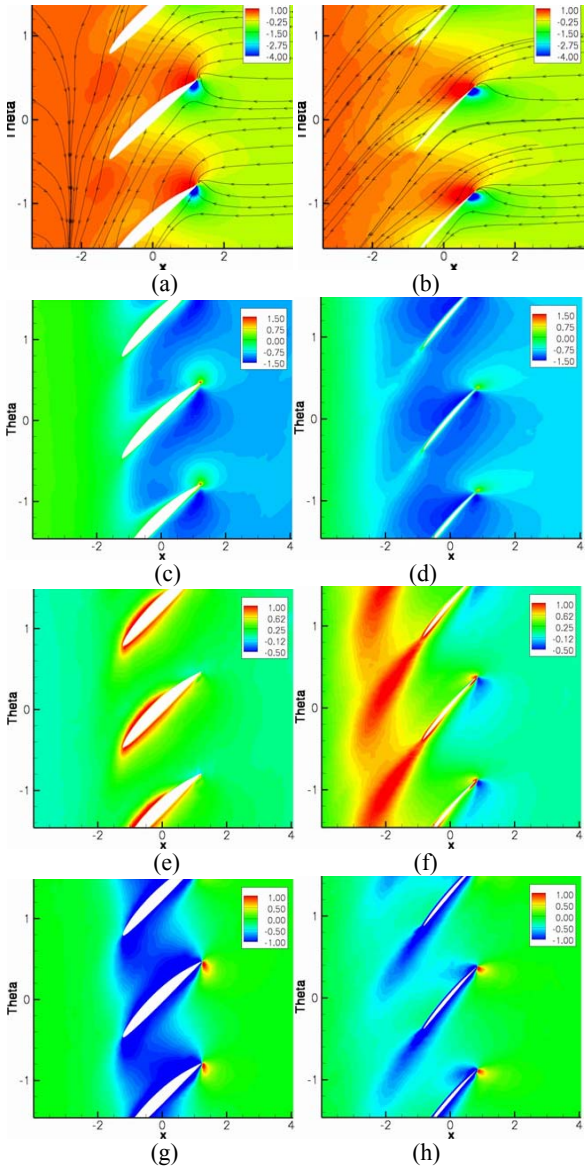

Figure 9. Time averaged flow fields in cross-planes at constant radii: (a) pressure with streamlines at r=0.4R, (b) pressure with streamlines at r=0.8R, (c) axial velocity at r=0.4R, (d) axial velocity at r=0.8R, (e) radial velocity at r=0.4R, (f) radial velocity at r=0.8R, (g) tangential velocity at r=0.4R (h) tangential velocity at r=0.8R.

propulsor at this location. These results are consistent with patterns of streamlines in figure 6.

Figure 9 shows time averaged flow fields in cross-planes at constant radii. The figures on the left Left figures are obtained at r = 0.4R and the figures on the right are given at r = 0.8R. The cross-section of a blade looks like an airfoil. In crashback condition, the leading and trailing edges of propulsor blades exchange their roles. Since the sharp trailing edge becomes the leading

edge in the condition, the large flow separations could occur at the sharp leading edge. The large flow separations can cause high amplitude fluctuations of unsteady loads. In figure 9(a) and 9(b), pressure contours with streamline are displayed. Sharp leading edges and large flow separations are shown in those figures. Angle of attack is larger at r=0.4R than at=r=0.8R. Figure 9(c) and 9(d) are axial velocities. The reversed flow near blade tips (r=0.8R) is high until downstream of the blade. The radial and tangential velocities show definite distinctions at those radii. At r=0.4R, the tangential velocity is high around blade surfaces, but the radial velocity only exist near blades. On the other hand, both of the radial and tangential velocities at r=0.8R are strong at the downstream of blades.

Two Quantities for Pressure Contributions to Thrust and Side-force

The pressure distribution on blade surfaces is very important to understand blade loadings because viscous force is much smaller than pressure force at high Reynolds number.

The pressure force exerted on propulsor surfaces is

$$\vec{F} = \sum_{f=\text{faces on surface}} p\,\vec{n}_f A_f \qquad (6)$$

where p is the pressure, $\vec{n}_f$ is the outward normal vector of the face, A_f is the area of the face, and the force vector $\vec{F}$ is summed up over all faces on the propulsor surface.

The thrust and the side-force are as follows.

$$(\text{Thrust}) = \vec{F}\cdot\vec{i} = \sum_{f=\text{faces}} p\,(\vec{n}_f\cdot\vec{i})A_f \qquad (7)$$

$$(\text{Side force}) = \sqrt{(\vec{F}\cdot\vec{j})^2 + (\vec{F}\cdot\vec{k})^2} = \sum_{f=\text{faces}} |p|\sqrt{(\vec{n}_f\cdot\vec{j})^2 + (\vec{n}_f\cdot\vec{k})^2}\,A_f \qquad (8)$$

Eq. (7) and (8) mean that $p\,(\vec{n}_f\cdot\vec{i})$ and $|p|\sqrt{(\vec{n}_f\cdot\vec{j})^2 + (\vec{n}_f\cdot\vec{k})^2}$ can be the effective pressure for thrust and side-force, respectively. So, those two quantities for pressure contributions to thrust and side-force are derived such as:

$$\alpha_f = (\vec{n}_f\cdot\vec{i})$$
$$\beta_f = \sqrt{(\vec{n}_f\cdot\vec{j})^2 + (\vec{n}_f\cdot\vec{k})^2} \qquad (9)$$

However, those quantities α_f and β_f should be invariant with the rotation because our system has the propulsor rotation. The quantity for thrust α_f is obviously not affected by the rotation. The quantity for side-force β_f can be proved by following derivation.

$$\begin{pmatrix}\vec{j}'\\ \vec{k}'\end{pmatrix} = \begin{pmatrix}\cos\theta & -\sin\theta\\ \sin\theta & \cos\theta\end{pmatrix}\begin{pmatrix}\vec{j}\\ \vec{k}\end{pmatrix} \qquad (10)$$

$$\sqrt{(\vec{n}_f\cdot\vec{j}')^2 + (\vec{n}_f\cdot\vec{k}')^2}$$
$$= \sqrt{((\vec{n}_f\cdot\vec{j})^2 + (\vec{n}_f\cdot\vec{k})^2)(\cos^2\theta + \sin^2\theta)} \qquad (11)$$
$$= \sqrt{(\vec{n}_f\cdot\vec{j})^2 + (\vec{n}_f\cdot\vec{k})^2}$$

Once we have α_f and β_f for all faces of the propulsor surface, the effective pressure for thrust and side-force can be easily computed from pressure distribution.

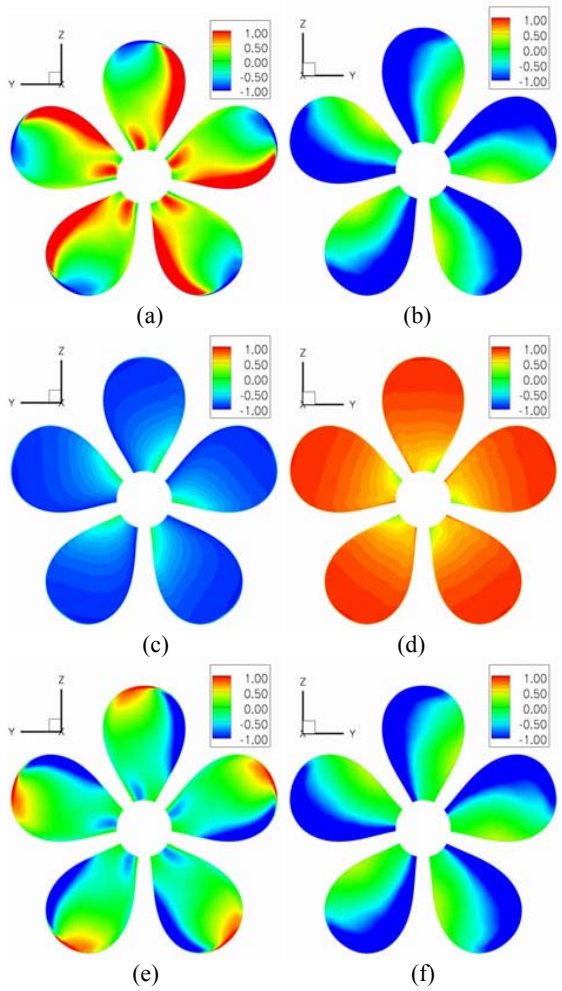

Figure 10. Pressure and effective pressure for thrust on blade surfaces: (a) pressure on pressure side, (b) pressure on suction side, (c) the quantity for thrust α_f on pressure side, (d) the quantity for thrust α_f on suction side, (e) effective pressure for thrust on pressure side, (f) effective pressure for thrust on suction side.

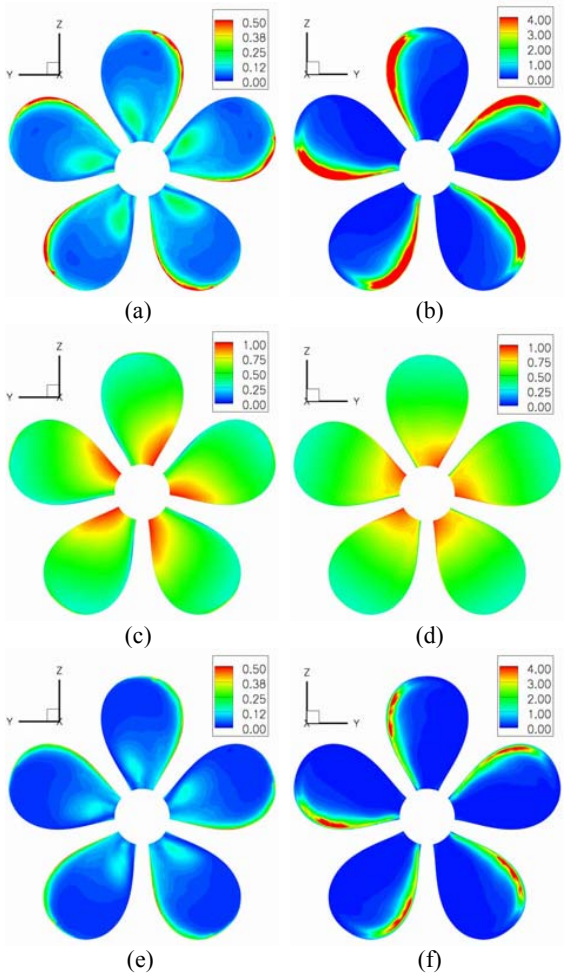

Figure 11. Pressure and effective pressure for side-force on blade surfaces: (a) RMS of pressure on pressure side, (b) RMS of pressure on suction side, (c) the quantity for side-force β_f on pressure side, (d) the quantity for side-force β_f on suction side, (e) RMS of effective pressure for side-force on pressure side, (f) RMS of effective pressure for side-force on suction side.

Figure 10 show pressure and effective pressure for thrust on blade surfaces. The time averaged pressure is plotted on pressure side (forward face) and suction side (aft face) in figure 10(a) and 10(b), respectively. The value of α_f on pressure side is almost negative in figure 10(c) and that on suction side is almost positive in figure 10(d). The magnitude of α_f is smaller at the root of blades because normal vectors of faces at that region are nearly perpendicular to the axial direction. The effective pressure for thrust is computed in figure 10(e) and 10(f). The effective pressure for thrust on pressure side looks opposite to the pressure on that side with the multiplication of α_f. We can predict the location where thrust is generated with this effective pressure. The negative thrust mainly originates the leading edge of suction side. The leading edge of pressure side also provides the negative thrust.

Figure 11 show RMS of pressure and effective pressure for side-force on blade surfaces. RMS of pressure is plotted on pressure side and suction side in figure 11(a) and 11(b), respectively. The RMS of pressure is much higher at the leading edge of the suction side and also quite higher at the leading edge of the pressure side. On both of pressure and suction side, the value of β_f is larger at the root of blades in figure 11(c) and 11(d). The RMS of effective pressure for side-force is computed in figure 11(e) and 11(f). Since β_f is smaller at the blade tip than at the root of blades, the RMS of effective pressure at tip becomes smaller,

but it is still high. So, the side-force is mainly generated from the leading edge of suctions side near the tip as the thrust does. However, the leading edge of pressure side does not affect the side-force significantly.

Conditional Averages for Thrust and Side-force

Chang et al. (2008) investigated the physics of high- and low- amplitude of thrust and side-force. In order to understand the physics, they looked at instantaneous flow fields at a high amplitude event and a low amplitude event. This approach gives us qualitative understandings of those events. However, this investigation was performed at a couple of extreme events and we cannot guarantee that those extreme events represent all of high- and low- amplitude events. The technique of conditional average (Antonia, 1981) can provide more quantitative information.

First, mean values and standard deviations of K_T and K_S are computed for a period of 38.1 revolutions. Black lines in figure 12 represent the smaller period for the conditional average. Blue lines in figure 12 mean that conditional averages are performed in this interval. When the magnitude of K_T is higher than that of $<K_T>-(K_T)'$, flow variables are separately averaged only for high thrust. Similarly, conditionally averaged fields for low thrust, high side-force, and low side-force are also obtained during 14.3 revolutions.

The effective pressures for thrust and side-force are applied to conditional averaged fields. The effective pressure for thrust on blade surfaces with conditional average is shown in figure 13. The region for negative thrust is wider both on pressure and suction side in high thrust averaging than in low thrust averaging. The negative thrust also comes from roots of blades on pressure side in high thrust averaging.

In figure 14, the effective pressure for side-force is plotted with the conditional average of side-force. The effective pressure is higher in high side-force averaging at the leading edge on suction side. The conditional average of side-force does not show significant difference compared to that of thrust.

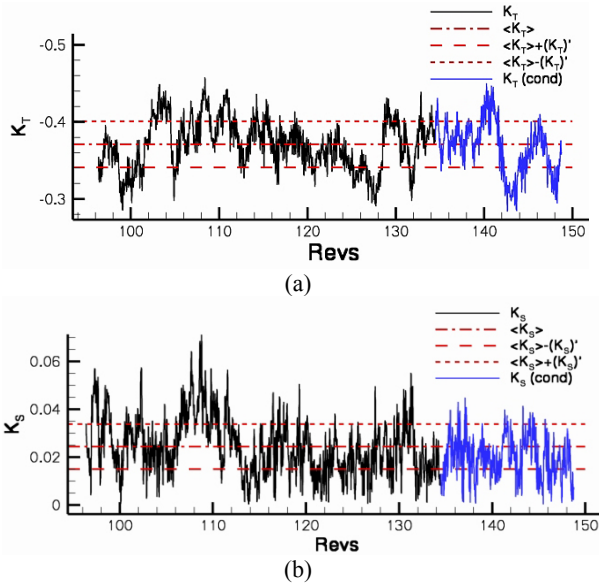

Figure 12. Time histories of unsteady loads for conditional average: (a) thrust coefficient K_T, (b) side-force coefficient K_S (black line is used to calculate mean and standard deviation for conditional average, and blue line means that conditional average is performed in this interval.)

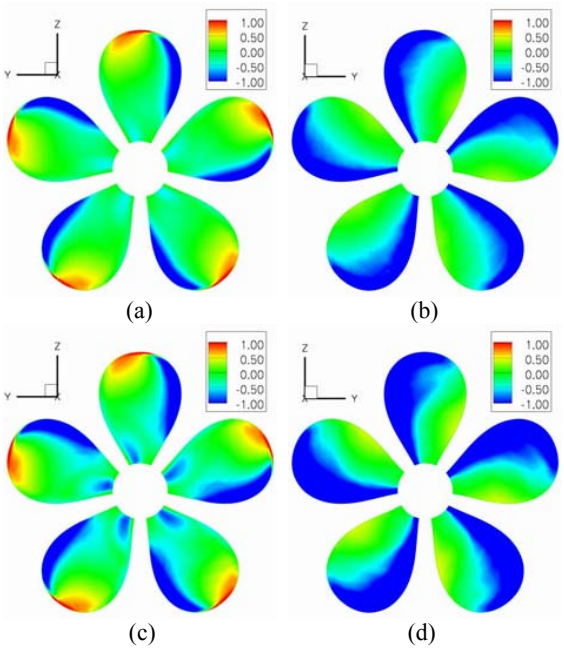

Figure 13. Effective pressure for thrust on blade surfaces: (a) on pressure side at high K_T, (b) on suction side at high K_T, (c) on pressure side at low K_T, (b) on suction side at low K_T.

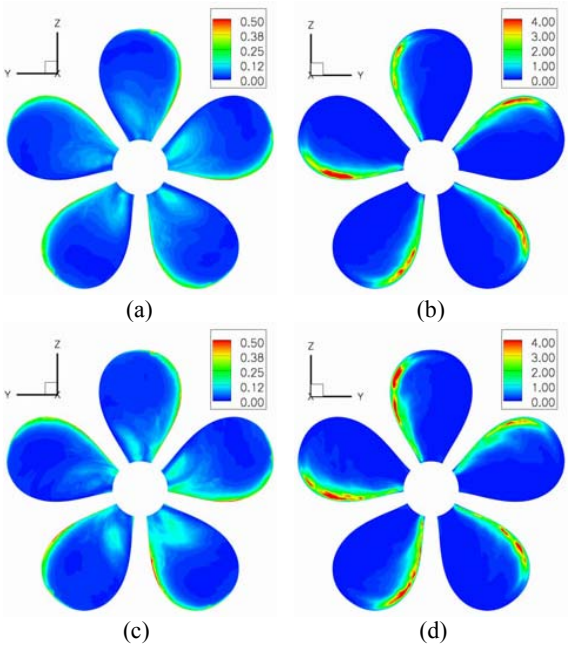

Figure 14. Effective pressure for side-force on blade surfaces: (a) on pressure side at high K_S, (b) on suction side at high K_S, (c) on pressure side at low K_S, (b) on suction side at low K_S.

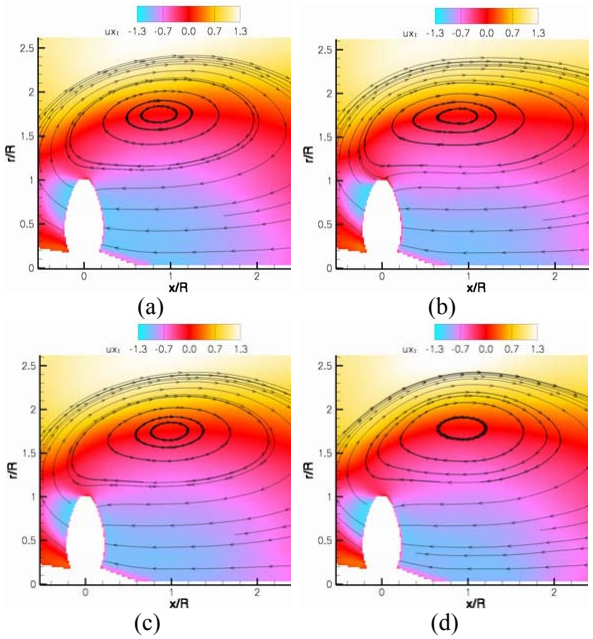

Figure 15. Circumferentially averaged axial velocity: (a) low K_T, (b) high K_T, (c) low K_S, (d) high K_S.

Figure 15 compares circumferentially averaged axial velocities with streamlines for low thrust, high thrust, low side-force, and high side-force averaging. Four figures with the conditional averages look very similar, but the high thrust averaging predicts slightly closer recirculation zone in the axial direction and the center of recirculation zone for the high side-force is located slightly outward of the propulsor in the radial direction. Table 4 quantitatively enumerates locations of centers of recirculation zone with those conditional averages.

Pressure contours with streamlines in cross-planes at constant radii are plotted in figure 16. Figure 16(a)-(b) are at r/R=0.4 and figure 16(c)-(d) are at r/R=0.8. The figures on the left (16(a) and 16(c)) are obtained for the low thrust average and the figures on the right (16(b) and 16(d)) are for the high thrust. Most noticeable observations for the figures are the larger angle of attacks and the stronger flow separations at the leading edges for high thrust. It implies that the large flow separations due to the large angle of attack could generate the large amplitude of thrust.

Figure 17 shows time averaged velocity fields at r/R = 0.8. Axial velocities for low and high thrust are very similar in figure 17(a)-(b). However, the radial and tangential velocities are different at the downstream and the suction side of blades. For the high thrust, the flow rate of the incoming flow is higher at the leading edge on the suction side and that of the outgoing flow is higher at the downstream of the blades. Also, the swirling motions are higher on the suction side for the high thrust.

	x_cen / R	r_cen / R
Average	0.93	1.75
Low K_T	0.87	1.75
High K_T	0.92	1.75
Low K_S	0.97	1.75
High K_S	0.93	1.79

Table 4. Locations of centers of recirculation zones of circumferentially averaged flow fields with conditional averages.

CONCLUSIONS

Flow around propulsor 4381 under crashback condition has been simulated with a new improved computational grid using the large eddy simulation methodology. The simulation has been performed at the advance ratio J=-0.7 and Re=480,000. The simulation yields agreeable mean values of unsteady loads as compared to experiments. Also, good agreement with experiments is observed in circumferentially averaged

flow fields. Two quantities for pressure contributions to thrust and side-force are introduced to more clearly understand the sources of thrust and side-force. Thrust and side-force are mainly generated from the suction side of the leading edge of propulsor blades. Conditional averages are performed for obtaining quantitative information about the complex flow physics of high or low thrust and high or low side-force.

ACKNOWLEDGEMENTS

This work was supported by the United States Office of Naval Research under ONR Grant N00014-05-1-0003 with Dr. Ki-Han Kim as technical monitor. Computing resources were provided by the Arctic Region Supercomputing Center of HPCMP, the Minnesota Supercomputing Institute, and MEnet of University of Minnesota. We are grateful to Dr. Stuart Jessup and Dr. Martin Donnelly for providing us with experimental data.

REFERENCES

Antonia, R., A., "Conditional Sampling in Turbulence Measurement", Annual Review of Fluid Mechanics, Vol. 13, 1981, pp. 131-156.

Beddhu, M., Taylor, L. K., Whitfield, D. L., "Strong Conservative Form of the Incompressible Navier-Stokes Equations in a Rotating Frame with a Solution Procedure", Journal of Computational Physics, Vol. 128, 1996, pp. 427-437.

Chang, P., Mahesh, K., "Large Eddy Simulation of Crashback in Marine Propulsors", Proceedings of the 26th Symposium on Naval Hydrodynamics, Rome, Italy, September 2006.

Chen, B., Stern, F., "Computational Fluid Dynamics of Four Quadrant Marine Propulsor Flow", Journal of Ship Research, Vol. 43, No. 4, 1999, pp. 218-228.

Davoudzadeh, F., Taylor, L. K., Zierke, W. C., Dreyer, J. J., McDonald, H., Whitfield. D. L., "Coupled Navier-Stokes and Equations of Motion Simulation of Submarine Maneuvers, Including Crashback", Proceedings of the 1997 ASME Fluids Engineering Division Summer Meeting, Vol. 2, ASME, New York, 1997.

Germano, M., Piomelli, U., Moin, P., Cabot, W. H., " A dynamic Subgrid-Scale Eddy Viscosity Model", Physics of Fluids A, Vol. 3, No. 7, 1991, pp. 1760-1765.

Jiang, C. W., Dong, R. R., Lui, H. L., Chang, M. S., "24-inch Water Tunnel Flow Field Measurements During Propulsor Crashback", 21st Symposium on Naval Hydrodynamics, The National Academies Press, Washington, DC, 1997, pp. 136-146.

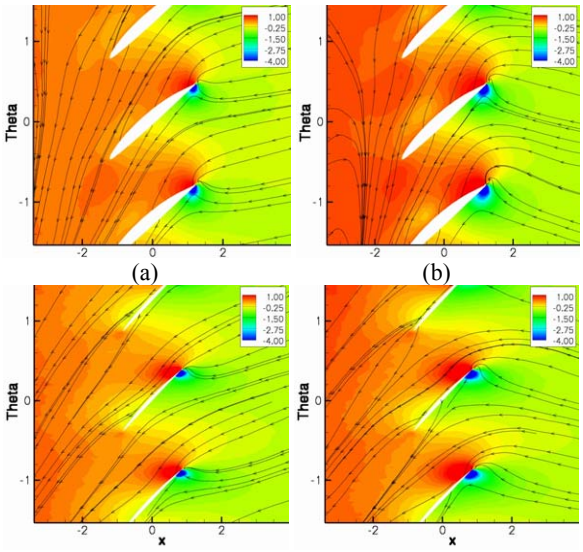

Figure 16. Pressure contours with streamlines in cross-planes at constant radii: (a) at r/R=0.4 for low K_T, (b) at r/R=0.4 for high K_T, (c) at r/R=0.8 for low K_T, (d) at r/R=0.8 for high K_T.

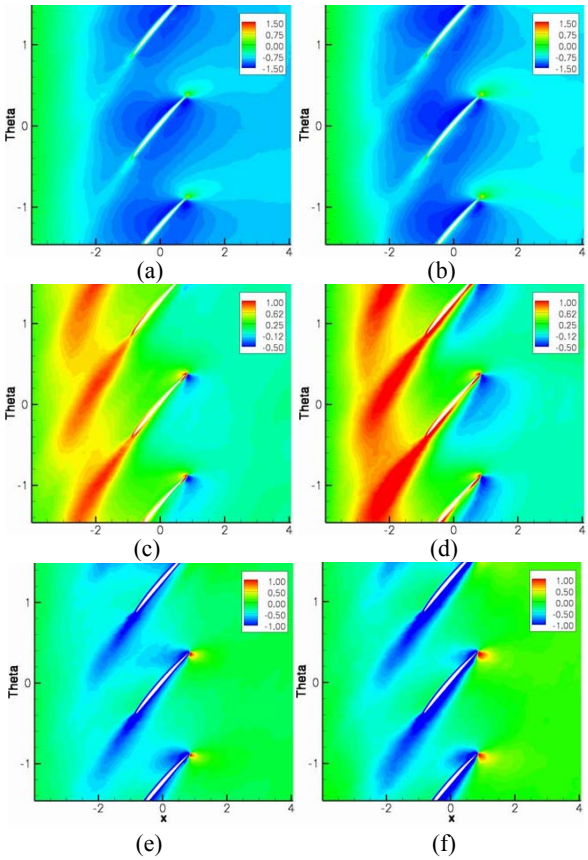

Figure 17. Time averaged velocity fields in cross-planes at r/R=0.8: (a) axial velocity for low K_T, (b) axial velocity for high K_T, (c) radial velocity for low K_T, (d) radial velocity for high K_T (e) tangential velocity for low K_T, (d) tangential velocity for high K_T.

Jessup, S., Chesnakas, C., Fry, D., Donnelly, M., Black, S., Park, J., "Propulsor Performance at Extreme Off Design Conditions", Proceedings of the 25th Symposium on Naval Hydrodynamics, St. John's, Canada, August 2004.

Jessup, S., Fry, D., Donnelly, M., "Unsteady Propulsor Performance in Crashback Conditions With and Without Duct", Proceedings of the 26th Symposium on Naval Hydrodynamics, Rome, Italy, September 2006.

Lilly, D. K., "A Proposed Modification of the Germano Subgrid-Scale Closure Model", Physics of Fluids A, Vol. 4, No. 3, 1992, pp. 633-635.

Majety, K., S., "Solutions to the Navier-Stokes Equations in Non-Inertial Reference Frame", PhD thesis, Mississippi State University, 2003.

Mahesh, K., Constantinescu, G., Moin, P., "A Numerical Methods for Large-Eddy Simulation in Complex Geometries", Journal of Computational Physics, Vol. 197, No. 1, 2004, pp. 215-240.

Vyšohlíd, M., Mahesh, K., "Large Eddy Simulation of Crashback in Marine Propulsors", Proceedings of the 26th Symposium on Naval Hydrodynamics, Rome, Italy, September 2006.